pubs.acs.org/Biomac Article

On the Mechanism of Self-Assembly by a Hydrogel-Forming Peptide

Gabriel A. Braun,* Beatrice E. Ary, Alexander J. Dear, Matthew C. H. Rohn, Abigail M. Payson, David S. M. Lee, Robert C. Parry, Connie Friedman, Tuomas P. J. Knowles, Sara Linse,* and Karin S. Åkerfeldt*

Cite This: https://dx.doi.org/10.1021/acs.biomac.0c00989 Read Online

ACCESS | Metrics & More | Article Recommendations | Supporting Information

ABSTRACT: Self-assembling peptide-based hydrogels are a class of tunable soft materials that have been shown to be highly useful for a number of biomedical applications. The dynamic formation of the supramolecular fibrils that compose these materials has heretofore remained poorly characterized. A better understanding of this process would provide important insights into the behavior of these systems and could aid in the rational design of new peptide hydrogels. Here, we report the determination of the microscopic steps that underpin the self-assembly of a hydrogel-forming peptide, SgI_{37-49}. Using theoretical models of linear polymerization to analyze the kinetic self-assembly data, we show that SgI_{37-49} fibril formation is driven by fibril-catalyzed secondary nucleation and that all the microscopic processes involved in SgI_{37-49} self-assembly display an enzyme-like saturation behavior. Moreover, this analysis allows us to quantify the rates of the underlying processes at different peptide concentrations and to calculate the time evolution of these reaction rates over the time course of self-assembly. We demonstrate here a new mechanistic approach for the study of self-assembling hydrogel-forming peptides, which is complementary to commonly used materials science characterization techniques.

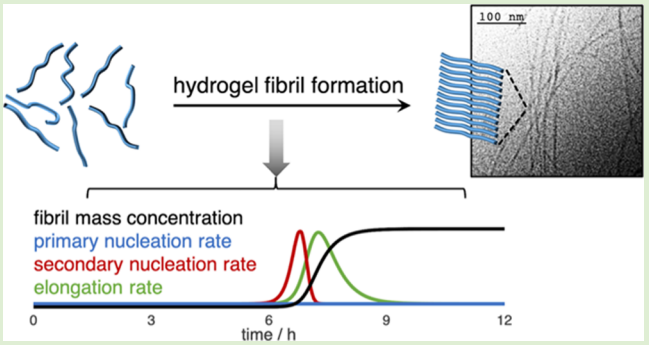

INTRODUCTION

Hydrogels are a class of soft materials consisting of a three-dimensional network of soluble, cross-linked fibrils which trap water to form a viscoelastic structure. There is a great level of chemical diversity within the class of hydrogels: common hydrogel-forming materials include proteins, peptides, polysaccharides, synthetic organic polymers, and hybrid organic–inorganic polymers.[1,2] The manner in which these subunits are linked to form the gel matrix can vary as well. The water-soluble fibrils can be composed of either covalently linked polymers or noncovalently linked supramolecular assemblies,[3] while the cross-linking between fibrils can be achieved through both covalent bonds and noncovalent interactions, such as hydrogen bonding, $\pi-\pi$ stacking, and van der Waals forces.[4] In systems that form supramolecular fibrils capable of non-covalent cross-linking, hydrogelation can proceed spontaneously (Figure 1A). Such gels typically have highly tunable characteristics and display self-healing properties.[5,6]

Peptide-based hydrogels, which are generally capable of spontaneous gelation, have attracted significant interest for use in biomedical applications, including wound dressing, tissue engineering, and drug delivery.[7] Peptides make ideal building blocks for biocompatible functional hydrogels: they readily form highly structured assemblies and the chemical diversity provided by the constituent amino acids allows for facile tuning of the gel properties.[8] In this study, we focus on a hydrogel-forming peptide, SgI_{37-49} (Figure 1B), derived from the human protein semenogelin I. A truncated version of this peptide, SgI_{38-48}, was previously shown to form a pH-dependent gel composed of β-sheet fibrils.[9] Despite containing a high level of sequence diversity, with 11 different amino acids represented in the 13-residue peptide, the SgI_{37-49} sequence follows a simple alternating pattern of hydrophobic and hydrophilic residues, resulting in an amphiphilic peptide with high β-sheet propensity. This motif of alternating polar and nonpolar residues is common in designed hydrogel-forming peptides, which generally employ a small set of amino acid types arranged in a repeating pattern.[8,10] Classic examples of designed amphiphilic hydrogel-forming peptides include the RADA/EAK16,[11−13] MAX,[14,15] and P_{11}[16,17] peptide families. Indeed, much of the progress over the past 20 years in understanding spontaneous gel-forming systems has come from investigations into these designed peptide amphiphiles.[18−20]

Received: June 27, 2020
Revised: October 8, 2020

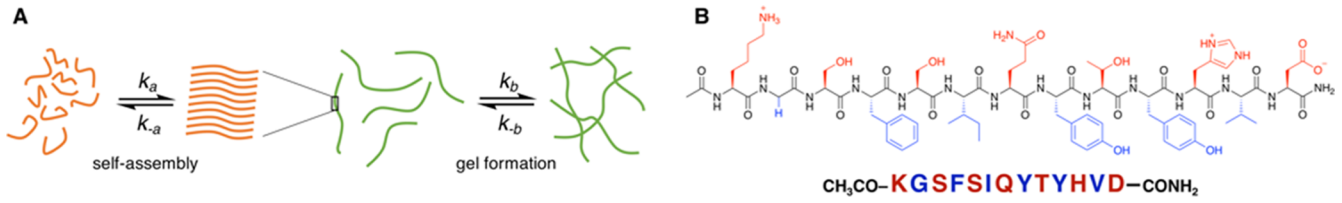

Figure 1. (A) Schematic of spontaneous gel formation. Monomeric peptides (orange) self-assemble to form ordered fibrils (green), which noncovalently cross-link to form the gel matrix. These two processes are coupled, but the exact timescale of each depends on the values of the rate constants k_a, k_{-a}, k_b, and k_{-b}. (B) $SgI_{37\text{-}49}$, the amphiphilic, hydrogel-forming peptide used in this study, with alternating hydrophilic (red) and hydrophobic (blue) residues.

The physical properties of peptide-based hydrogels, including fibril morphology and the mesh size, strength, and elasticity of the gel, are routinely studied; these investigations typically employ techniques such as rheometry, small-angle scattering measurements, transmission electron microscopy (TEM), and atomic force microscopy.[21−24] Although the structural and material properties of a gel are undeniably important, the dynamic period of self-assembly and cross-linking that leads to the formation of the gel matrix is a rich, yet comparatively understudied source of complementary information about a gel-forming system.[25,26] The majority of kinetic investigations have focused on noncovalently cross-linked hydrogels using techniques such as time-resolved rheological and ion mobility measurements to determine the kinetics of cross-linking between fibrils to form the gel matrix.[27−29] In addition, a smaller number of studies have investigated the kinetics of fibril formation, often relating it to the kinetics of gel formation.[29−31] In these studies, fibril formation is typically monitored by observation of the development of secondary structure as a function of time using either direct methods such as circular dichroism[29,32,33] (CD) and Fourier transform infrared[34] (FTIR) spectroscopy or indirect methods such as thioflavin T (ThT) fluorescence,[9,30,31] which, if carefully calibrated, quantitatively reports on fibril mass concentration.[35] These studies have largely focused on the timescale of fibril formation, however, without attempting to deduce the underlying mechanism of self-assembly.

A better understanding of the mechanism of self-assembly is of great interest, as it would provide insights into the kinetic and thermodynamic determinants of fibril formation, which govern the gel material properties.[15,25,26,36] Previous studies have elucidated interactions and reaction intermediates that are crucial to the self-assembly processes of various hydrogel-forming peptides using techniques such as mass spectrometry, X-ray diffraction, and ^{1}H NMR spectroscopy.[37−39] In particular, these studies demonstrated the importance of hydrophobic interactions and $\pi-\pi$ stacking in disparate peptide systems, indicating the general involvement of these interactions in the self-assembly of hydrogel-forming peptides.[30,38−40] The self-assembly of hydrogel-forming peptides is moreover often dependent on both pH and ionic strength, indicating the importance of limited electrostatic repulsion.[41−44] Several previous studies of the kinetics of hydrogel fibril formation have observed the presence of a long lag phase during which the extent of self-assembly is below the signal-to-noise ratio of most techniques,[45,46] followed by a growth phase in which the fibril mass concentration increases rapidly; this led to the conclusion that self-assembly in these systems proceeds through a nucleated reaction.[9,27,47−49] Furthermore, several studies have highlighted a set of possible mechanistic steps, including monomer conformational changes[14,16,50,51] and hierarchical self-assembly steps in which one-dimensional aggregates associate laterally to form various complex, higher-order structures.[16,52,53] The opposite chemical kinetics approach, which takes as a starting point a set of experimental data and finds a minimal set of composite microscopic steps underlying the formation of fibrillar assemblies, which can explain all data, has to our knowledge not been reported for hydrogel-forming systems.

The fundamental mechanisms of linear polymerization involved in the formation of unbranched filamentous aggregates, such as those found in many peptide-based hydrogels,[26] are well documented.[54−56] In these systems, fibril formation occurs through two interrelated processes: the generation of new fibril nuclei through nucleation, and the growth of these nuclei to form longer fibrils. In principle, the self-assembly of a peptide to form a fibril within a hydrogel network is described by a combination of these well-established nucleation and growth mechanisms. There is a long history of the determination of the steps underlying protein and peptide aggregation, particularly in the context of protein misfolding diseases: in the 1970s, such studies revealed the specifics of the aberrant aggregation of the hemoglobin S (HbS) mutant involved in sickle cell anemia,[57−60] while more recent studies have used similar approaches to study β-amyloid (Aβ) peptides,[61,62] α-synuclein,[63] tau,[64] and polyglutamine repeat (polyQ) peptides.[65,66] In this context, the framework of chemical kinetics has proved to be a powerful tool for elucidating assembly mechanisms, and the availability in the past 10 years of rate laws for different classes of fibrillar growth processes has unlocked the potential to use this tool to understand the formation of peptide and protein filaments.[67−69]

In this study, we report the determination of the mechanism of fibril formation during the hydrogelation of $SgI_{37\text{-}49}$, as well as the rate constants and reaction orders for the processes involved. As direct methods of observing β-sheet formation, such as CD or FTIR spectroscopy, cannot reliably be used with $SgI_{37\text{-}49}$ because of light scattering from the self-assembled aggregates,[9] we follow fibril formation indirectly using ThT as a fluorescent reporter dye. Using integrated rate laws corresponding to the different mechanisms of filamentous self-assembly, we then relate these kinetic aggregation data to the underlying steps involved in $SgI_{37\text{-}49}$ fibril formation. Although in the late stages of self-assembly at high peptide concentrations the kinetic aggregation profile displays features consistent with reduced aggregation rate, likely caused by gel formation and impeded diffusion, the $SgI_{37\text{-}49}$ aggregation process can nevertheless be well described by the existing rate laws for filamentous self-assembly. From this data analysis, we

https://dx.doi.org/10.1021/acs.biomac.0c00989
Biomacromolecules XXXX, XXX, XXX−XXX

are able to generate a quantitative description of the self-assembly of SgI_{37-49}.

MATERIALS AND METHODS

Materials. All solvents and reagents were purchased from commercial suppliers and used without further purification. Rink resin was purchased from ChemPep. *N*,*N*,*N*′,*N*′-Tetramethyl-*O*-(1*H*-benzotriazol-1-yl)uronium hexafluorophosphate (HBTU) and all Fmoc-protected amino acids were purchased from Advanced Chem Tech. Diethyl ether (99.0%) and acetonitrile were purchased from EMD Millipore and Pharmaco-Aaper, respectively. Sodium deuteroxide (NaOD) (30% w/v, 99.5% D) and deuterium oxide (D_2O) (99.9% D) were purchased from Cambridge Isotope Laboratories. Hydrochloric acid (HCl) (36.5−38%) was obtained from EM Industries, while acetic acid (AcOH) (99−100%) and ammonium hydroxide (NH_4OH) (25%) were purchased from VWR Chemicals. ThT was purchased from Calbiochem. Piperidine (≥95.5%), *N*,*N*-dimethylformamide (DMF) (99.8%), piperazine (98%), acetic anhydride (≥99%), trifluoroacetic acid (TFA) (99%), 1,2-ethanedithiol (≥98%), anisole (99.7%), thioanisole (≥99%), guanidine hydrochloride (GuHCl) (99%), and deuterium chloride (DCl) (35% w/v, 99% D) were purchased from Sigma-Aldrich.

Peptide Synthesis and Purification. SgI_{37-49}, CH_3CO-(KGSFSIQYTYHVD)-$CONH_2$, was synthesized using solid-phase Fmoc chemistry, employing a Gyros Protein Technologies Tribute peptide synthesizer. A Rink amide resin (0.1 mmol, 0.43 mmol/g) was used to provide a C-terminal carboxamide. Each amino acid was double-coupled to reduce the chance of deletion mutants, with each coupling using 5 molar equivalents of amino acid in a 1:1 mixture with HBTU as a coupling reagent. Fmoc deprotection was achieved using 20% piperidine in DMF. The peptide N-terminus was acetylated by treatment with 2 mL acetic anhydride. The peptide was lyophilized and cleaved from the resin by incubation with stirring for 2 h at room temperature in 5 mL of a 4.5/0.25/0.15/0.1 volume mixture of TFA/1,2-ethanedithiol/anisole/thioanisole. The resin was separated from the peptide by vacuum filtration and washed three times with 5 mL TFA. The filtrate was concentrated with a stream of argon gas. The crude peptide was precipitated with the addition of ice-cold diethyl ether and collected by vacuum filtration. The off-white precipitate was then washed with diethyl ether (2 × 5 mL), dissolved in a 1:1 mixture of water and acetonitrile, then frozen, and lyophilized. The identity of the peptide was confirmed by liquid chromatography−mass spectrometry, with electrospray ionization MS in positive mode using an Agilent G6125BW LCMS (Figure S1). Crude peptide was purified by high-performance liquid chromatography (HPLC) (Agilent 1100) in 5 mg/mL injections on a C18 column (Grace Vydac #218TP101522, 250 × 22 mm, 10−15 μm). A linear gradient of 15−40% solvent B over 25 min at 10 mL/min (solvent A: 0.1% TFA in water; solvent B: 0.1% TFA in 9:1 acetonitrile/water) was used (Figure S2).

Cryo-TEM. Pure peptide was dissolved in water, and the concentration was determined by absorbance at 280 nm (ε_{280} = 2800 M^{-1} cm^{-1}, based on the presence of two tyrosine residues), with readings taken in triplicate. The peptide was then diluted to a final concentration of 1.0 mM, and the pH was adjusted to 8.0 using NaOH. The sample was allowed to incubate at room temperature for 24 h, and gelation was confirmed by visual inspection.

The electron microscopy sample was prepared in a controlled environment vitrification system to maintain stable temperature and to minimize solution loss during sample preparation. The sample was prepared as a thin liquid film, <300 nm thick, on lacey carbon-filmed copper grids. This was plunged into liquid ethane at −180 °C to vitrify the sample; this minimizes water crystallization as well as component segmentation and rearrangement, thus maintaining original microstructures. The vitrified sample was stored under liquid nitrogen until measured. An Oxford CT3500 cryo-holder and its workstation were used to transfer the specimen into the electron microscope (Philips CM120 BioTWIN Cryo), which was equipped with a postcolumn energy filter (Gatan GIF100). The acceleration voltage was 120 kV, and the images were recorded digitally with a CCD camera under low electron dose conditions.

FTIR Spectroscopy. To exchange residual trifluoroacetate anions for chloride anions, the purified, lyophilized peptide was weighed and dissolved in water, to which was added 13.7 molar equivalents of concentrated HCl (calculated assuming that the lyophilized product is 70% peptide by weight); the solution was then frozen and relyophilized. The lyophilized, anion-exchanged peptide was redissolved in D_2O and the concentration was determined by absorbance at 280 nm, with readings taken in triplicate. The sample was diluted to the desired concentration with D_2O, and the pH was corrected to 5.5 using NaOD and, if needed, DCl. The sample was incubated at room temperature for 1 week to allow for the pH to drift to ca. 8.0.

FTIR spectra were obtained using a Bruker Optics Vertex 70 FTIR spectrometer with a photovoltaic mercury cadmium telluride detector, using OPUS software. For each scan, 30 μL of the sample was loaded into a Harrick 13 mm diameter demountable liquid cell with CaF_2 windows and a path length set to 56 μM using a Teflon spacer. Spectra were generated between 900 and 4000 cm^{-1} at 2 cm^{-1} resolution with 512 scans per sample. The background was subtracted using a D_2O sample incubated for the same duration as the peptide. The baseline of the amide I region was flattened by subtraction of a third-degree polynomial fit to the spectrum between 1550 and 1850 cm^{-1}, excluding the amide I region between 1580 and 1720 cm^{-1}. Second derivative analysis was performed on the unprocessed spectrum.

Kinetic Aggregation Assays. Pure monomeric peptide was obtained by gel filtration: between 0.5 and 2 mg lyophilized peptide was dissolved in 250 μL of 6 M GuHCl, pH 3.5, injected onto a Superdex Peptide 10/300 GL column (GE Healthcare), and eluted with an isocratic 0.5 mL/min flow of 5.0 mM AcOH, pH 3.5 (Figure S3). The monomeric peptide was collected on ice in 0.3−0.5 mL fractions using low-binding Eppendorf tubes (Axygen). Fraction collection excluded both the very beginning and the very end of the monomer elution, as these might contain low-molecular-weight aggregates and GuHCl, respectively. Fraction concentration, measured in triplicate by absorbance at 280 nm using a Nanodrop 2000 instrument (Thermo Fisher), typically varied between 25 and 300 μM. Fractions with sufficiently high concentration (generally those above 50 μM) were combined, and the concentration of the combined fractions was measured in triplicate by absorbance at 280 nm. The pH of the peptide solution was adjusted to 8.0 using NH_4OH and AcOH (if needed); ThT was added from a 1.1 mM stock solution to a final concentration of 25 μM (preliminary tests indicate that ThT in the concentration range 20−50 μM does not perturb the kinetics of SgI_{37-49} self-assembly; see Figure S4). A dilution series was prepared, working in low-binding Eppendorf tubes on ice, using 5 mM AcOH buffer with 25 μM ThT, pH 8.0 (adjusted with NH_4OH). Each concentration was plated in quintuplicate, with 90 μL per well, in a black, clear-bottomed, PEG-coated 96-well half-area plate (Corning 3881), which was sealed with a clear plastic film.

Kinetic aggregation assays were performed using a BMG Labtech FLUOstar Omega microplate reader at 37 °C under quiescent conditions. ThT fluorescence was measured through the bottom of the plate using an excitation filter of 440 nm and an emission filter of 480 nm, with measurements taken every 120 s. Data were collected over a period of 2−4 days.

Kinetic Aggregation Assay Data Analysis. Kinetic aggregation data were preprocessed using the free online AmyloFit program (www.amylofit.ch.cam.ac.uk).[70] The time period of interest for each sample was selected, starting at time zero and extending until the fluorescence signal reaches a plateau. Each data set was normalized, averaging over 10−15 data points for the zero-point offset and 25−50 points for the end-point normalization.

The aggregation half-times were calculated by performing a linear fit to the normalized fluorescence data for the time during which the signal intensity was between 0.4 and 0.6. The half-time was taken to be the time at which the linear fit equals 0.5. As determined prior to the experiment, the number of data sets for each concentration was reduced from 5 to 3 by choosing the quintuplicates with lowest

https://dx.doi.org/10.1021/acs.biomac.0c00989
Biomacromolecules XXXX, XXX, XXX−XXX

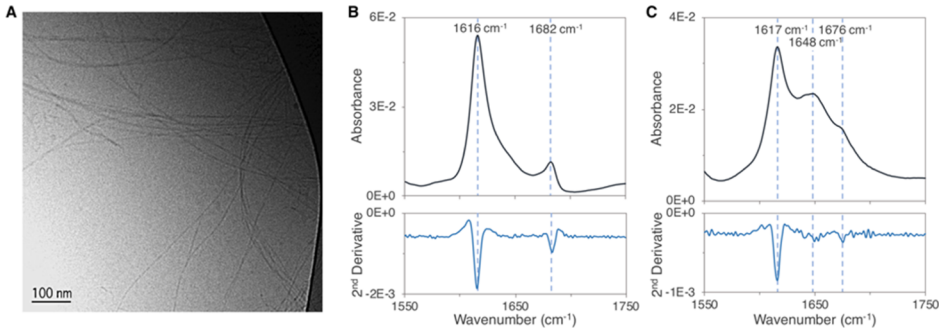

Figure 2. Structural analysis of SgI_{37-49} assemblies. (A) Cryo-TEM of the fibril network formed by SgI_{37-49} at 1.0 mM. The FTIR amide I region of (B) 2.0 mM SgI_{37-49} and (C) 100 μM SgI_{37-49}, including both the absorbance spectrum and the second derivative (in blue). Bands around 1620 and 1680 cm^{-1} are consistent with the β-sheet secondary structure.[72,73] The signal at 1648 cm^{-1} in the 100 μM sample is indicative of the random coil.

standard deviation in half-time values (except for the 41 μM sample, for which only one useable data set was obtained); these data sets were then used as technical triplicates for data analysis. Linear fitting of the double-logarithmic half-time data was performed separately for concentrations above and below the saturation threshold of 50 μM to determine the scaling exponent, γ, for each concentration range. The values t_{lag} and t_{growth} (Figure 5A) were calculated from the normalized kinetic aggregation data, with t_{lag} defined as the time during which the normalized fluorescence intensity was less than 0.1 and t_{growth} defined as the time during which the normalized fluorescence intensity was between 0.1 and 0.9.

Fitting of kinetic models to the data was performed using AmyloFit. To start, unseeded, nonsaturating models were fit to data below the saturation threshold. For the primary and secondary nucleation-dominated models, initial guesses for the parameters n_c and n_2 were calculated from the half-time plot scaling exponent, with $n_c \approx -2\gamma$ and $n_2 \approx -(2\gamma + 1)$. To roughly determine the magnitude of combined rate constants, the reaction order parameters (n_c and n_2, when applicable) were set to global constants and the combined rate constants (k_+k_n for all models and k_+k_2 and k_+k_- for models including secondary nucleation and fragmentation, respectively) were set to global fits, varying the initial guesses widely. To expedite this process, a low number of basin hops (typically between 3 and 5) were used. Once approximate magnitudes for the combined rate constants were found that gave decent fits, the number of basin hops was gradually increased to improve the fit. At this point, the reaction order parameters could also be changed to global fitting parameters to improve the goodness of fit. If this resulted in a significant change in the values of all parameters and an overall decrease in the goodness of fit, the combined rate constant parameters were set as global constants while the reaction order parameters were fit. This process was repeated iteratively until the best possible fit to a given model was found.

For the fitting of secondary nucleation-dominated models including saturating processes to kinetic aggregation data of all concentrations, the initial guesses for the reaction order and rate constant parameters were based on the values obtained through fitting of the nonsaturating secondary nucleation-dominated model to the below-saturation data. Fitting using kinetic models including saturation of secondary nucleation and saturation of elongation was performed in AmyloFit. Initial guesses for the Michaelis constant parameter for each model (K_E for the saturating elongation model and K_M for the model including saturating secondary nucleation) were calculated as $K_E \approx m_0$ and $K_M \approx (m_0)^{n_2}$, where m_0 is the concentration at which the relevant process is half-saturated ($V = V_{max}/2$). Optimization of the fit proceeded as described above. The kinetic model including saturation of all processes was used as previously reported by Dear et al.[71]

A more detailed and comprehensive discussion of the AmyloFit data fitting process, as well as the integrated rate laws off of which the models are based, can be found in the program protocol.[70]

RESULTS

SgI_{37-49} Fibril Characterization. Cryo-TEM images, obtained for 1.0 mM SgI_{37-49}, reveal that the peptide self-assembles to form a loose network of regular fibrils (Figure 2A). The fibrils have a diameter of ca. 6 nm, with length in the micrometer range, and are mainly present as single fibrils, although some laterally associated fibrils are observed. The amide I region of the FTIR spectrum, recorded at a concentration of 2.0 mM SgI_{37-49}, displays a high-intensity band at 1616 cm^{-1} and a low-intensity band at 1682 cm^{-1} (Figure 2B). The frequencies and relative intensities of these bands are characteristic of the β-sheet secondary structure.[72,73] In the FTIR spectrum for 100 μM SgI_{37-49} (Figure 2C), both these bands are present, indicating that the β-sheet is still the predominant secondary structure at the end stage of the kinetic assays used in this study. In addition to these characteristic β-sheet bands, there is a broad band centered around 1648 cm^{-1}, which is indicative of a random coil. This likely reflects the presence of nonaggregated peptide, which represents a much larger fraction of the total peptide in the 100 μM sample than in the 2.0 mM sample.

Mechanisms of Self-Assembly. The overall rate of peptide fibril formation is dependent on the microscopic processes that underpin this self-assembly. These events can be divided into processes that increase the total fibril mass concentration and processes that increase the total number of fibrils (Figure 3).

The increase in fibril mass concentration is typically driven almost entirely by the growth of existing aggregates, which occurs through the elongation of protofibrils and fibrils by the addition of monomers to their termini.[74,75] A description of the origin of the increase in the total number of aggregates is more complex, as there are several possible mechanisms by which new fibrils can form. Primary nucleation, which is the non-fibril-catalyzed association of monomers to form stable aggregates, is the only entirely monomer-dependent mechanism of new fibril formation.[45] Classically, this is described as a homogeneous, uncatalyzed reaction; primary nucleation may also be heterogeneous, however, in cases where the formation of a nucleus is catalyzed by a surface such as the vessel wall, a phospholipid membrane, or the air−water interface.[76] There also exist self-replicating mechanisms of new fibril formation, in which the existing fibrils catalyze the formation of new fibril nuclei. This can either take the form of secondary nucleation, a process in which monomers nucleate on the surface of the existing fibrils,[77] or fragmentation, where the existing aggregates break apart to form multiple smaller fibrils, thus

https://dx.doi.org/10.1021/acs.biomac.0c00989
Biomacromolecules XXXX, XXX, XXX−XXX

Mechanism	Elongation	Primary Nucleation	Secondary Nucleation	Fragmentation
Increase in fibril number	–	$k_n m(t)^{n_c}$	$k_2 m(t)^{n_2} M(t)$	$k_- M(t)$
Increase in fibril mass	$2k_+ m(t) P(t)$	negligible	negligible	–
Monomer dependent	✓	✓	✓	✗
Fibril dependent	✓	✗	✓	✓
Saturation effects	✓	✓	✓	✗

Figure 3. Main processes of filamentous self-assembly. The first and second rows specify the manner in which each process affects the total number of fibrils and the total fibril mass concentration as a function of time. The parameters k_+, k_n, k_2, and k_- are the rate constants for elongation, primary nucleation, secondary nucleation, and fragmentation, respectively. The parameters n_c and n_2 are the reaction orders for primary and secondary nucleation. The time-dependent variables $m(t)$, $M(t)$, and $P(t)$ represent the monomer concentration, total fibril mass concentration, and fibril number concentration, respectively. Also shown is the dependence of each process on monomer and fibril concentration, as well as whether the process can saturate at high peptide concentration.

exposing additional growth sites.[78] The rate of secondary nucleation is dependent on the concentration of both monomers and fibrils in solution, while fragmentation, being a monomer-independent process, depends only on the concentration of fibrils.

Because of the differences in the physical nature of the events that underly these self-assembly phenomena, the rate of each process has a characteristic dependence on the monomer concentration. Consequently, global fitting of kinetic models derived from rate laws corresponding to these different mechanisms to kinetic aggregation data can be used to determine which of these processes contribute significantly to the peptide self-assembly.[61,70] From this fitting, the rate constants and reaction orders for each relevant process can be determined, thus providing additional insights into the self-assembly process.

Kinetic Aggregation Assays. It is necessary to obtain highly pure peptide for kinetic aggregation assays, as even trace impurities can affect the rate of self-assembly. Consequently, after initial purification by high-performance liquid chromatography (Figure S2), the peptide was subjected to further purification by size exclusion chromatography (Figure S3) immediately before self-assembly was initiated through a temperature jump from 0 to 37 °C, thus creating a supersaturated state. This final purification step was intended to separate the monomeric peptide from any preformed aggregates, whose presence catalyzes fibril formation in systems with self-replication pathways. Self-assembly was monitored using ThT, whose fluorescence was found to scale linearly with the total aggregate concentration in the concentration range used (Figure S5).

The aggregation of SgI_{37-49} was followed in this manner for solutions with a starting monomer concentration in the range of 30–97 μM (Figure 4). SgI_{37-49} self-assembly is characterized by a long lag phase, during which there is no apparent change in the total fibril mass concentration above the signal-to-noise ratio, followed by a very steep growth phase, in which fibril formation occurs very quickly (Figure 5A). The sharply sigmoidal curve shape of the SgI_{37-49} kinetic aggregation data

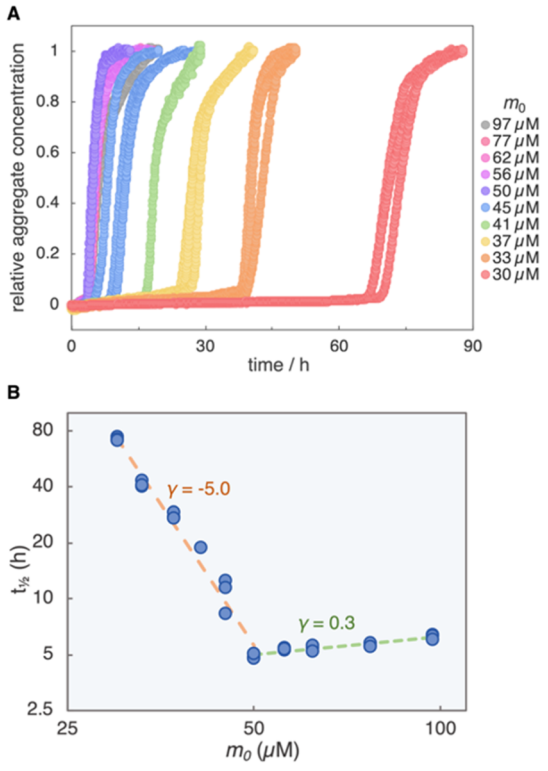

Figure 4. SgI_{37-49} kinetic aggregation data at 37 °C in 5.0 mM ammonium acetate, pH 8.0. (A) Normalized aggregation curves for the initial monomer concentration range 30–97 μM. (B) Double-logarithmic plot relating the time at which half of the final fibril mass concentration was reached ($t_{1/2}$) to the starting monomer concentration (m_0).

was found to be highly reproducible. This is readily seen in the replicates of the 30, 33, and 37 μM samples in Figure 4; this reproducibility was also observed between repeats of the whole experiment.

At low initial monomer concentrations, the length of the lag phase displays a strong concentration dependence. At concentrations above 50 μM, however, the duration of the lag phase appears to be concentration-independent. This is seen as a positive curvature of the double-logarithmic half-time plot (Figure 4B), which relates the half-time, $t_{1/2}$, to the starting monomer concentration, m_0, where the half-time is defined as the time at which the total fibril mass concentration reaches half of its final value. The strong negative slope in the half-time plot at lower concentrations indicates a highly concentration-dependent rate of self-assembly, while the flat line at higher concentrations indicates the sharp loss of this dependence; this behavior is indicative of the presence of enzyme-like saturation effects.[62] The loss of the concentration dependence of SgI_{37-49} aggregation above ca. 50 μM was found to be highly reproducible. Such behavior might also be caused by the possible increased generation of nonfibrillar, off-pathway aggregates at high peptide concentrations,[79] although it is unlikely that at higher concentrations, SgI_{37-49} would generate a significant population of amorphous aggregates, as the β-sheet character of the system continues to increase with concentration even above 50 μM, as seen through both ThT fluorescence (Figure S5) and FTIR spectroscopy (Figure 2B,C).

Mechanisms of SgI_{37-49} Self-Assembly. We first focused on the aggregation process below the saturation concentration,

https://dx.doi.org/10.1021/acs.biomac.0c00989
Biomacromolecules XXXX, XXX, XXX–XXX

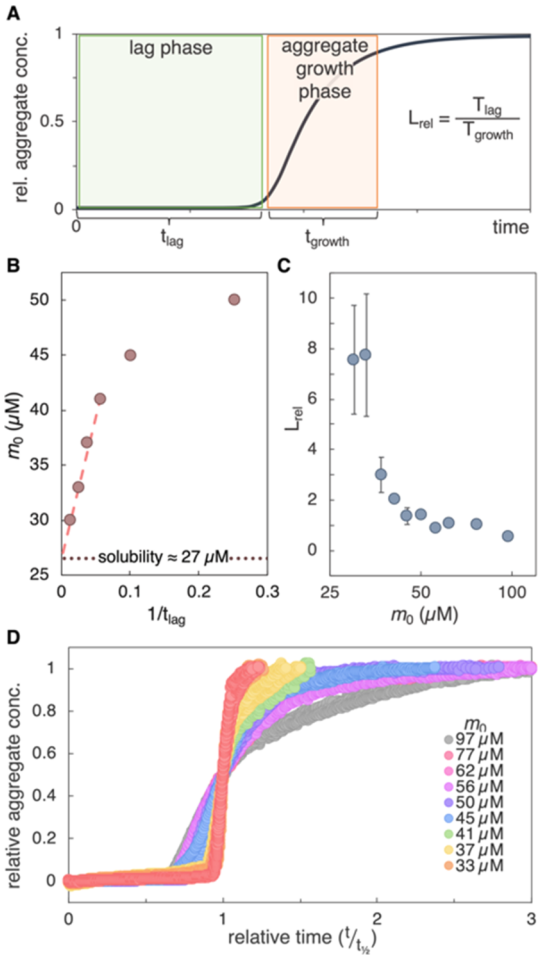

Figure 5. (A) Representative self-assembly profile, with the lag phase (green) and the aggregate growth phase (orange) highlighted. The duration of each phase (t_{lag} and t_{growth}) is marked below the time axis; these values are related through the parameter L_{rel}. (B) Initial monomer concentration, m_0, vs $1/t_{lag}$. The y-intercept of a straight line fit to the low-concentration linear regime indicates that the solubility of $SgI_{37\text{-}49}$ in 5.0 mM ammonium acetate, pH 8.0, is ca. 27 μM. (C) L_{rel} as a function of m_0. (D) $SgI_{37\text{-}49}$ kinetic aggregation curves shown in Figure 4A, with the time axis scaled to $t_{1/2}$ for each data set.

50 μM $SgI_{37\text{-}49}$, in the initial analysis to determine the mechanisms involved in $SgI_{37\text{-}49}$ self-assembly.

The solubility of $SgI_{37\text{-}49}$ was estimated by plotting the initial monomer concentration as a function of $1/t_{lag}$ (Figure 5B), where t_{lag} is the duration of the lag phase. On this graph, extrapolation of $1/t_{lag} = 0$ yields the saturation concentration intercept, indicating the concentration at which the lag time diverges, as is required at the solubility limit. This analysis indicates that the solubility of $SgI_{37\text{-}49}$ in 5.0 mM ammonium acetate, pH 8.0, is ca. 27 μM. This concentration represents the critical aggregation concentration, above which the solution is supersaturated and self-assembly will occur. This value is consistent with observations from the kinetic assays, in which no self-assembly could be detected over periods of up to 4 days at concentrations lower than 25 μM.

The sharply sigmoidal aggregation profile of $SgI_{37\text{-}49}$ (Figure 4A) indicates a very high level of cooperativity and is characteristic of self-assembly dominated by a secondary, fibril-catalyzed mechanism of fibril formation. During the initial lag phase, when self-assembly is not observable by ThT fluorescence, low levels of aggregates are slowly formed through both fibril-independent and fibril-dependent processes. Once a critical mass of aggregates has formed, the rate of the self-replicating secondary mechanism increases sharply, leading to the observed exponential growth phase. A more comprehensive and quantitative treatment of the time evolution of the different self-assembly processes throughout $SgI_{37\text{-}49}$ fibril formation is shown in Figure 8.

This sigmoidal aggregation profile can be qualitatively characterized by calculating the relative duration of the lag and exponential growth phases. This can be done through the parameter L_{rel}, defined as $L_{rel} = t_{lag}/t_{growth}$, where t_{lag} is the duration of the lag phase and t_{growth} is the duration of the period in which the majority of the total aggregate growth occurs (Figure 5A).[80] The possible values of L_{rel} for a given system are governed by the mechanisms underpinning self-assembly. In a system for which the evolution is determined by a single timescale, as is the case for a system containing only primary, non-fibril-catalyzed pathways, L_{rel} will be constant at all concentrations, as both the lag time and the growth time depend on this single timescale.[80,81] For $SgI_{37\text{-}49}$, however, L_{rel} varies with concentration (Figure 5C), indicating that the kinetics of $SgI_{37\text{-}49}$ self-assembly are governed by multiple timescales. This can be directly visualized by normalizing the time axis of each of the kinetic aggregation curves to $t_{1/2}$ (Figure 5D). In systems for which the kinetics of self-assembly are governed by a single timescale, these time-normalized curves will align in a single master curve.[81] The time-normalized $SgI_{37\text{-}49}$ aggregation curves do not align in this manner, however, demonstrating that self-assembly here depends on multiple timescales. These analyses indicate that the $SgI_{37\text{-}49}$ self-assembly proceeds through a secondary, fibril-catalyzed process, rather than through a simple primary nucleation and growth mechanism. The presence of a secondary mechanism of fibril formation was verified through seeding experiments, in which varying concentrations of preformed fibrils were added to a solution of monomeric peptide, which was then allowed to self-assemble. The addition of seed fibrils resulted in a decrease in the observed lag phase (Figure S6), which is consistent with the presence of a fibril-catalyzed, self-replicating process.

The half-time plot (Figure 4B), which concisely shows the dependence of the self-assembly rate on the starting monomer concentration, provides insights into which of the two main fibril-catalyzed processes (secondary nucleation and fragmentation) are present. The concentration dependence of the aggregation half-time is typically described by the power law $t_{1/2} \sim m_0^{\gamma}$.[61] In the double-logarithmic plot, this relationship becomes $\ln(t_{1/2}) \sim \gamma \ln(m_0) + c$, with the scaling exponent γ equal to the slope. The magnitude of the scaling exponent reports on the monomer dependence of the dominant aggregation processes. A scaling exponent of $\gamma = -1/2$ is characteristic of a fragmentation-dominated system, while a scaling exponent of $\gamma < -1/2$ is indicative of a system dominated either by primary nucleation ($\gamma \approx -n_c/2$) or secondary nucleation ($\gamma \approx -(n_2 + 1)/2$), where n_c and n_2 are the reaction orders of the primary and secondary nucleation mechanisms, respectively.[70] For $SgI_{37\text{-}49}$ below 50 μM, $\gamma = -5.0 \pm 0.2$. The magnitude of γ thus rules out fragmentation as a possible primary mechanism of new fibril formation, as it indicates that the rate of $SgI_{37\text{-}49}$ self-assembly is too strongly dependent on the initial monomer concentration to be dominated by the monomer-independent fragmentation

https://dx.doi.org/10.1021/acs.biomac.0c00989
Biomacromolecules XXXX, XXX, XXX−XXX

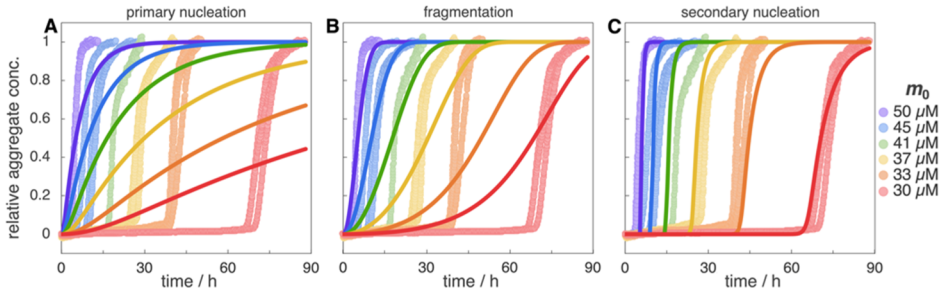

Figure 6. Global fitting of nonsaturating kinetic models to kinetic aggregation data below 50 μM. (A) A model including primary nucleation as the only mechanism of new fibril formation provides poor fits at all concentrations. (B) Fragmentation-dominated model poorly fits all but the highest concentrations. (C) Model including secondary nucleation as the dominant mechanism matches both the lag and exponential growth phases at all concentrations.

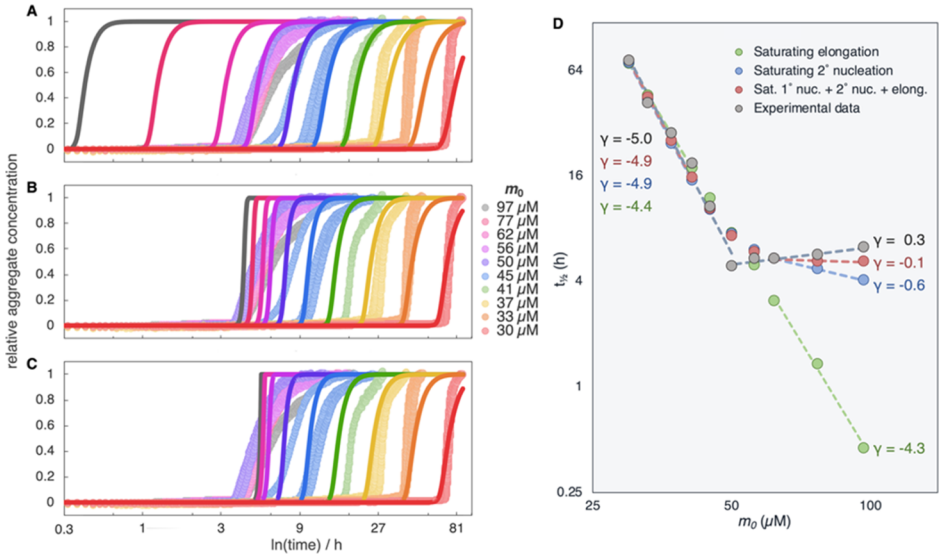

Figure 7. Global fitting of secondary nucleation-dominated models including saturation effects to aggregation data from all concentrations (30−97 μM). Models include saturation of (A) elongation, (B) secondary nucleation, and (C) all self-assembly mechanisms. Time is displayed here on a logarithmic scale to facilitate comparison of the fits to high concentration data; this results in exaggeration of the fitting errors at earlier times. (D) Comparison of the experimental half-times with those generated by the fits shown in (A−C).

process. Consequently, having ruled out both primary nucleation and fragmentation as principal mechanisms of new fibril formation, it can be concluded that $SgI_{37\text{-}49}$ self-assembly is dominated by secondary nucleation.

This conclusion is supported by fitting of kinetic models of nonsaturating self-assembly to the kinetic aggregation data below 50 μM using the program AmyloFit (Figure 6).[70] A model including secondary nucleation as the main self-replication process is capable of matching both the long lag phases and sharp exponential growth at all concentrations, whereas neither primary nucleation- nor fragmentation-dominated models are able to provide a good global fit.

Saturation of Self-Assembly Processes. Having determined through analysis of $SgI_{37\text{-}49}$ aggregation behavior below 50 μM that $SgI_{37\text{-}49}$ self-assembly proceeds through a secondary nucleation-dominated mechanism, it then becomes possible to determine which mechanism is responsible for the saturating effects observed above 50 μM. Saturation is possible in processes that include a catalytic step, making saturation analogous to what is observed in enzyme kinetics, as typically described by the Michaelis−Menten model. In all self-assembly processes, the monomeric peptide acts as the equivalent of the substrate of an enzymatic reaction. Although homogeneous primary nucleation is an uncatalyzed reaction and so cannot saturate, heterogeneous primary nucleation can saturate, with the catalytic surface acting as the enzyme-like species.[71] For elongation and secondary nucleation, the ends and sides of the fibril act as the enzyme analogues, respectively.[75,77,82] At concentrations below the saturation threshold, the rate of all of these processes is limited by the association of monomers to the catalytic site, making the overall rate of the mechanism dependent on the concentration of the available monomer. Above the saturation threshold, however, the rate of these processes is limited by the rate at which the monomer rearranges to extend the fibril (in the case of elongation) or the newly formed nucleus detaches from the catalytic surface (in the case of primary and secondary nucleation). These steps do not depend on the concentration of the available monomer, making the overall rate of each process monomer-independent.

The change in the magnitude of the half-time plot scaling exponent, γ, between nonsaturating and saturating concentrations provides useful insights into which of these mechanisms includes a saturating step. The monomer dependence of elongation contributes approximately −1/2 to the scaling exponent, indicating that saturation of a step in the elongation mechanism will lead to an increase in γ of

https://dx.doi.org/10.1021/acs.biomac.0c00989
Biomacromolecules XXXX, XXX, XXX−XXX

approximately 1/2.[62] The contribution of the secondary nucleation mechanism to the scaling exponent in a secondary nucleation-dominated system, however, is proportional to half of the reaction order n_2, indicating that saturation of a step in the secondary nucleation process will lead to an expected increase in γ of $n_2/2$.[70] Knowing that $\gamma \approx -(n_2 + 1)/2$ for a secondary nucleation-dominated process, the reaction order n_2 for $SgI_{37\text{-}49}$ can be estimated to be ~9 from the low-concentration scaling exponent of $\gamma = -5.0$; this would lead to an anticipated $\Delta\gamma$ of around 4.5. The observed change in the magnitude of the scaling exponent for $SgI_{37\text{-}49}$ is $\Delta\gamma = 5.3$. The fact that $\Delta\gamma \gg 1/2$ clearly indicates that the saturation effects cannot be caused solely by the saturation of a step in the elongation process, indicating that the secondary nucleation mechanism must saturate.

Kinetic models accounting for saturation effects can be fit to the complete $SgI_{37\text{-}49}$ kinetic aggregation data set, including concentrations both above and below the saturation threshold (Figure 7). Each kinetic model fits the data well at low, nonsaturating concentrations. Above the saturation threshold, however, a model including only saturation of elongation (Figure 7A) provides a poor fit, while models including saturation of secondary nucleation (Figure 7B) and saturation of all processes (Figure 7C) describe the data much better. This is clearly shown by comparison of the half-times of the various fits (Figure 7D): while all models closely match the scaling exponent at low concentrations, the high-concentration scaling exponent of $\gamma = 0.3$ is better fit by the saturating secondary nucleation and all processes saturating models ($\gamma = -0.6$ and -0.1, respectively) than by the saturating elongation model ($\gamma = -4.2$).

Above 50 μM, the aggregation curves begin to overlap, leading to $\gamma > 0$ in this concentration range. Although none of the models used here fully replicate this phenomenon, such behavior is qualitatively consistent with saturation of all self-assembly processes. This is reflected to a degree in a reduced fitting error for the fully saturated model relative to that of the saturated secondary nucleation model (0.0315 and 0.0345, respectively), although this reduction in error does not fully demonstrate the improvement in fit because of the inability of the models to accurately capture the curve shapes at high concentration. The atypical high-concentration curve shapes suggest that an additional, unmodeled phenomenon is occurring. Nevertheless, from this fitting, it can be concluded that saturation of a step in the secondary nucleation process is primarily responsible for the observed loss of the concentration dependence of $SgI_{37\text{-}49}$ self-assembly (as demonstrated by the relatively good fit provided by the model including only saturation of secondary nucleation) but that elongation and primary nucleation must also be saturated in this concentration range. The fact that primary nucleation displays saturating behavior indicates that this process is necessarily a heterogeneous, surface-catalyzed reaction.

Physical Insights from Fitting Parameters. Beyond providing evidence of which mechanisms are involved in self-assembly, the data fitting also generates relevant values of the parameters for each process. It is worth noting that, although the decreased diffusion rate caused by gel formation has the potential to affect the kinetics of late-stage aggregation, this will have a relatively small impact on the accuracy of the kinetic parameters determined from the data fitting, as this information is largely derived from time points before $t_{1/2}$, when such gel-induced effects are negligible (see the Discussion section for a more detailed analysis of these effects). The parameters for the kinetic model including saturation effects in all processes (Figure 7C) are shown in Table 1. As mentioned previously, the parameter n_2 represents the reaction order for secondary nucleation. Because the rate of self-assembly from a solution of pure monomer depends only on the product of the molecular elongation rate constant (k_+) and those for primary nucleation (k_n) and secondary nucleation (k_2), only the effective rate constants k_+k_n and k_+k_2 can be determined. Because both the primary nucleation and elongation of $SgI_{37\text{-}49}$ were found to be largely saturated in the relevant concentration range, it was not possible to accurately determine their rates k_n and k_+, their respective Michaelis constants K_P and K_E, or the primary nucleation reaction order n_c. Instead, we can only accurately determine the products k_+K_E and $k_nK_P^{n_c}$, which correspond to the saturated rates for these processes, k'_+m_0 and $k'_nm_0^{n_c}$, respectively (see Dear et al.[71] for a discussion of these saturation-perturbed rate constants). Consequently, the rate constants for the various self-assembly processes were determined as $(k_+K_E)(k_nK_P^{n_c})$ and $(k_+K_E)k_2$. The Michaelis constant for the secondary nucleation mechanism, K_M, could be accurately determined, however, as this process saturates within the concentration range studied.

Table 1. Rate Constants and Reaction Orders for the Secondary Nucleation-Dominated Kinetic Model with Saturation Effects in All Mechanisms Fit to $SgI_{37\text{-}49}$ Aggregation Data (Figure 7C)

$(k_+K_E)(k_nK_P^{n_c})$ $(M^{-n_c}\ s^{-2})^a$	$(k_+K_E)k_2$ $(M^{-n_2-1}\ s^{-2})^a$	n_2	K_M (M^{n_2})	K_S (μM)
1×10^{-29}	3×10^{40}	10.7	1.1×10^{-46}	50

[a]Because of the late-time kinetic perturbations caused by hydrogelation, the rate constants could only be determined to order-of-magnitude accuracy (Figure S7).

The dominance of secondary nucleation in $SgI_{37\text{-}49}$ self-assembly is shown by the parameter $\varepsilon' = \lambda'^2/\kappa'^2$, which gives the rate of primary nucleation relative to that of secondary nucleation at a given concentration (Figure 8). λ' and κ' are

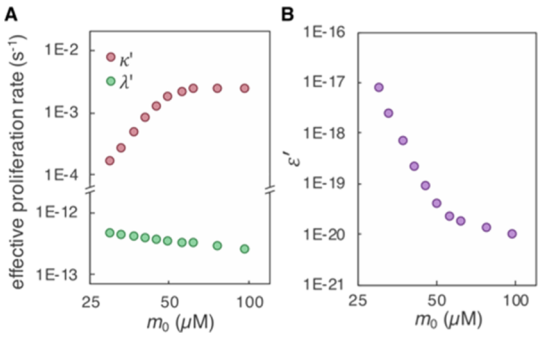

Figure 8. (A) λ' and κ', the effective catalytic proliferation rates through primary and secondary nucleation, respectively, at each concentration studied in the kinetic aggregation assays. (B) ε', which shows the rate of primary nucleation relative to that of secondary nucleation, at each concentration. Secondary nucleation becomes increasingly dominant with increasing monomer concentration, although this effect diminishes as secondary nucleation saturates. λ', κ', and ε' were calculated from the integrated rate law derived by Dear et al.[71] using the fitting parameters shown in Table 1.

https://dx.doi.org/10.1021/acs.biomac.0c00989
Biomacromolecules XXXX, XXX, XXX−XXX

the effective catalytic fibril proliferation rates via primary and secondary nucleation, respectively, and are given by $\lambda' = \sqrt{k_+' k_n' m_0^{n_c}}$ and $\kappa' = \sqrt{2k_+' k_2' m_0^{n_2+1}}$, where $k_+' k_n'$ and $k_+' k_2'$ are saturation-perturbed rate constants, as derived by Dear et al.[71] At all concentrations studied here, the value of ε' for $SgI_{37\text{-}49}$ is extremely small (on the order of 10^{-18} to 10^{-20}), demonstrating that secondary nucleation is many orders of magnitude more important than primary nucleation for the generation of new fibrils. The relative importance of secondary nucleation increases exponentially with increasing concentration because of the highly monomer-dependent nature of $SgI_{37\text{-}49}$ secondary nucleation. This trend diminishes as secondary nucleation saturates and becomes concentration-independent, although the rate of secondary nucleation remains many orders of magnitude greater than that of primary nucleation at all concentrations.

Because secondary nucleation is the dominant process in $SgI_{37\text{-}49}$ self-assembly, the value of the secondary nucleation reaction order, n_2, provides meaningful insights into the physical characteristics of this process. The reaction order reports on the monomer dependence of the rate-limiting step. For most secondary nucleation-dominated systems, in which nucleation is nonclassical,[83] the magnitude of n_2 corresponds to the extent of fibril surface coverage by monomeric peptide, with the magnitude of n_2 inversely related to the level of adsorption.[84] (Note that this differs from the case of classical nucleation, in which n_2 corresponds to the number of monomers required to form a critical nucleus.[85]) For $SgI_{37\text{-}49}$, the value of the secondary nucleation reaction order obtained through fitting is $n_2 = 10.7$. This is much larger than those found for other peptides that self-assemble to form β-sheet fibrils, such as $A\beta_{40}$, $A\beta_{42}$, and polyglutamine repeat peptides, for which $1 \leq n_2 \leq 4$.[61,62,86] The rate order of nucleation for $SgI_{37\text{-}49}$ is instead comparable to that of the aggregation-prone HbS mutant that causes sickle cell anemia, for which $n_2 \approx 11.4$.[87] This suggests that the level of monomer adsorption onto the fibril surface is very low, which is indicative of low affinity between monomeric and fibrillar species.[84]

From the Michaelis constant, K_M, the half-saturation concentration, K_S, can be calculated using the relationship $K_S = K_M^{1/n_2}$.[62] The half-saturation concentration represents the monomer concentration at which the rate of the saturated process is half of the fully saturated maximum rate. Using the fitting values obtained for K_M and n_2, the half-saturation concentration for the secondary nucleation of $SgI_{37\text{-}49}$ can be calculated to be $K_S = 50\ \mu M$, which matches the observed loss of concentration dependence in the aggregation rate at around 50 μM, as seen in the half-time plot (Figure 4B).

Time Evolution of Self-Assembly Reaction Rates. Using the rate laws for each self-assembly mechanism (Figure 3) and the parameters determined through fitting (Table 1), it is possible to calculate the rate of each process throughout $SgI_{37\text{-}49}$ fibril formation (Figure 9). The time evolution of these reaction rates provides a useful frame for understanding how each of these processes contributes to fibril formation. To allow for the decomposition of the effective rate constants k_+k_n and k_+k_2 and comparison of the rates of primary and secondary nucleation, it is necessary to estimate the elongation rate constant, k_+. Based on the fibril dimensions determined by cryo-TEM (Figure 2A), the saturation-perturbed elongation rate constant at 50 μM $SgI_{37\text{-}49}$ was estimated to be $k_+' = 2 \times 10^5\ M^{-1}\ s^{-1}$ (see the Supporting Information).

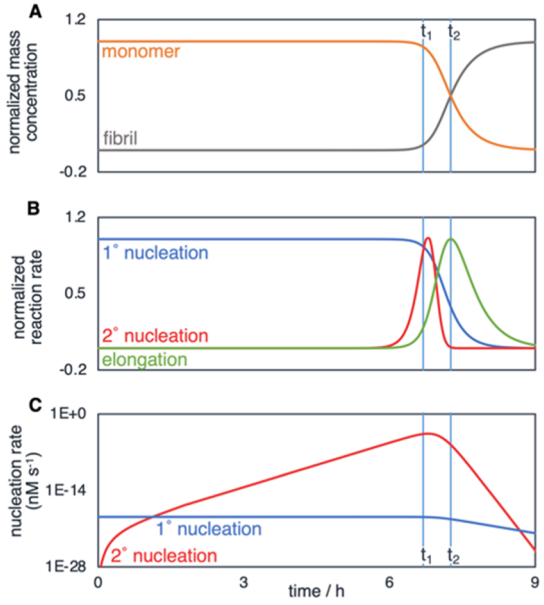

Figure 9. Time evolution of the concentration of various species and the rates of various processes throughout $SgI_{37\text{-}49}$ self-assembly. (A) Normalized mass concentration of monomeric peptide (orange) and self-assembled peptide (gray). (B) Normalized rates of primary nucleation (blue), secondary nucleation (red), and elongation (green). (C) Non-normalized rates of primary nucleation (blue) and secondary nucleation (red); rates are given in units of nM s^{-1} and shown on a logarithmic scale. In all plots, t_1 marks the end of the lag phase, when the increase in fibril mass concentration becomes macroscopically observable; t_2 indicates the half-time, when the fibril and monomer mass concentrations are equal, and the elongation rate is at its maximum. Fibril mass concentration was calculated for a 50 μM $Sg_{37\text{-}49}$ sample using the integrated rate law for fully saturated, secondary nucleation-dominated self-assembly[71] and the fitting parameters shown in Table 1. Reaction rates were calculated from the rate laws shown in Figure 3 using the parameters in Table 1.

At time zero, when the system consists of only monomeric peptide, the only active process is primary nucleation, as it is the only mechanism that does not require existing aggregates. The rate of secondary nucleation mechanism quickly becomes much greater than that of primary nucleation, however (Figure 9C). During the majority of the lag phase, the total amount of aggregated peptide remains relatively low; consequently, the fibril-dependent rate of secondary nucleation, although significantly higher than that of primary nucleation, remains low. Because little monomer is consumed during this period, the rate of primary nucleation remains essentially unchanged. As the total mass of aggregated peptide increases throughout the lag phase, the rate of the fibril-catalyzed secondary nucleation process increases exponentially. This generates a large number of new aggregates, leading to a corresponding, but slightly delayed, increase in the rate of elongation. This elongation eventually results in a sufficiently significant increase in the total mass concentration of self-assembled peptide such that aggregation becomes observable by ThT fluorescence (t_1); this marks the end of the lag phase and the start of the exponential growth phase.

The growth phase consists of the rapid consumption of the available monomer and a concurrent increase in total aggregate mass. Monomeric peptide is quickly consumed during the

https://dx.doi.org/10.1021/acs.biomac.0c00989
Biomacromolecules XXXX, XXX, XXX−XXX

growth phase, causing the rate of primary nucleation to fall. The rate of secondary nucleation, which is heavily dependent on monomer concentration, reaches its maximum shortly after the start of the growth phase. At the half-time of self-assembly (t_2), the elongation rate reaches its maximum. Following the midpoint of the exponential growth phase, the rates of all aggregation processes decrease as the monomer becomes completely depleted and the total aggregate mass reaches its final plateau.

DISCUSSION

In this study, we have successfully determined the mechanisms of self-assembly of a hydrogel-forming peptide, SgI_{37-49}, using kinetic models of filamentous aggregation. Nevertheless, there remain significant challenges in characterizing hydrogels in this manner, most significantly because of the changes in the system that occur during hydrogelation. We have focused so far entirely on fibril formation, without explicitly considering the effects that gelation might have on self-assembly. Previous studies have shown that the two processes are often functionally concurrent,[30−32] although in some systems there is a significant lag between fibril formation and gelation.[29,49] In cases where gel formation occurs on a similar timescale to fibril formation, the decreased diffusion rate caused by formation of the gel could have a significant impact on the kinetics of self-assembly. Although these effects would be minimal when few fibrils are present in the solution, they could become significant as the number of fibrils increases. For an unseeded reaction, such as those used in this study, this means that the self-assembly mechanism most affected would be elongation, as the rates of both primary and secondary nucleation reach their maxima at relatively low fibril concentrations, while the maximum rate of elongation is reached when the fibril concentration is relatively high (Figure 9B).

Indeed, the atypical curve shapes observed at high concentrations may be the result of changes in sample viscosity due to self-assembly. At concentrations above 50 μM, the aggregation half-time increases with concentration (Figure 4B), which is caused by lower rates of self-assembly during the latter stages of the aggregate growth phase at higher concentrations (Figure 10A). This is clearly reflected in the concentration dependence of t_{lag} and t_{growth} above the saturation threshold (Figure 10B). In this concentration range, t_{lag} remains essentially constant, while t_{growth} is longer

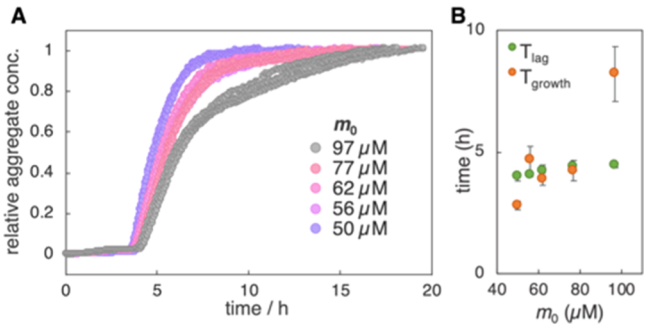

Figure 10. SgI_{37-49} self-assembly at concentrations above the saturation threshold (50−97 μM). (A) Normalized kinetic aggregation curves show that the self-assembly behavior differs most significantly during the late stages of the exponential aggregate growth phase. (B) In this concentration range, t_{lag} (green) is constant, while t_{growth} (orange) increases with peptide concentration.

at higher concentrations, demonstrating that the differences in the self-assembly behavior between these samples occur during the growth phase rather than the lag phase. The decreased rate of self-assembly is especially pronounced in the latter stages of the aggregate growth phase, which is consistent with the expected effects of hydrogelation, as explained above. The fact that this observed decrease in the rate of self-assembly scales with concentration is also consistent with the effects of hydrogelation, as a higher concentration of peptide would result in a denser gel matrix, which would increase the solution viscosity and decrease the mass transport, resulting in a decrease of the molecular rates of monomer-dependent steps in the aggregation pathway. This behavior cannot be explained through the models of fibrillar self-assembly used in this study, which do not account for changes in sample viscosity. However, as the insight provided by these kinetic fits comes largely from times before $t_{1/2}$, such late-time changes in viscosity do not preclude data fitting with these models, particularly in unseeded samples, as are used in this study. As such, the accuracy of the reaction orders and saturation constants determined through fitting is unaffected. These hydrogel-induced effects do sufficiently affect the kinetics of late-time self-assembly to limit determination of the rate constants to order-of-magnitude accuracy, however. This can be demonstrated by comparing the parameters generated from data fitting using the entire kinetic aggregation data set to the parameters generated from fitting only to times prior to any kinetic perturbations caused by hydrogelation (Figure S7).

The effects of hydrogel formation also help explain the challenges that were encountered in performing seeded kinetics experiments with SgI_{37-49}. Although catalytic seeding behavior was observed (Figure S6), these effects were much weaker than those previously reported for other systems with secondary nucleation-dominated mechanisms of self-assembly.[88] This muted seeding effect could be due in part to rapid gel formation by the seed fibrils. Although the mixing of the monomeric and seed peptide solutions would disrupt physical cross-links between seed fibrils, such cross-links have previously been shown to reform almost immediately.[32,89,90] The presence of these cross-linked seed fibrils would limit diffusion and consequently slow the rate of seeded nucleation.[91] This effect would be more pronounced at higher seed concentrations, which would offset the increased catalysis expected with higher concentrations of seeds. Additionally, it is unknown whether the catalytic function of fibrils might be affected if the fibril is part of a physically cross-linked network.

The effect of surfaces on self-assembly is another factor that must be considered in the kinetic studies of hydrogel fibril formation, as evidenced by the heterogeneous nature of SgI_{37-49} primary nucleation. Surfaces have been shown to be capable of both accelerating and retarding the self-assembly of peptides, depending on the characteristics of both the surface and the peptide.[91,92] Additionally, the air−water interface has been shown to facilitate peptide self-assembly.[93,94] Consequently, both the container material and shape may have significant effects on the kinetics of fibril formation. This represents an important consideration for mechanistic studies of hydrogel self-assembly: for example, the presence of significant surface effects may render some of the conclusions drawn from *in vitro* kinetic assays inapplicable to the process of *in vivo* hydrogelation. Although the effect of surfaces and interfaces introduces additional variables to kinetic investigations of fibril formation, such studies can also be used to

https://dx.doi.org/10.1021/acs.biomac.0c00989
Biomacromolecules XXXX, XXX, XXX−XXX

better understand how different surfaces affect self-assembly behavior,[95,96] which could be useful in the optimization of the performance of functional hydrogels.

In short, there are a number of factors that present challenges for the development of mechanistic descriptions of hydrogel self-assembly. In particular, the changes in the solution environment that accompany hydrogelation represent an intrinsic and potentially significant obstacle to the characterization of hydrogel-forming systems. The development of kinetic models of filamentous self-assembly that account for changes in viscosity and diffusion rate during the course of aggregation would greatly facilitate mechanistic investigations of hydrogel fibril formation. However, this study proves that it is still possible to characterize the steps involved in hydrogel fibril formation using currently available kinetic theories of linear fibril formation.

CONCLUSIONS

In this study, we have revealed that the self-assembly of the hydrogel-forming peptide SgI_{37-49} is governed by the secondary nucleation of monomers on the surface of existing fibrils. This catalytic nucleation process displays enzyme-like saturation effects, with the rate of nucleation being highly concentration-dependent below 50 μM and effectively concentration-independent at higher concentrations. Fitting of kinetic models of filamentous self-assembly to kinetic aggregation data provided rate constants and reaction orders for all self-assembly processes. From this, the rate of each mechanistic step throughout the course of fibril formation was determined, providing a detailed, time-resolved picture of the process of SgI_{37-49} fibril formation.

To our knowledge, this represents the first comprehensive description of the specifics of self-assembly from a monomeric to an essentially one-dimensional aggregated state in a hydrogel-forming system. The approach used in this study is complementary to techniques commonly used to study hydrogels, such as rheometry and microscopy, as it provides quantitative insights into the dynamic process preceding gel formation, which has remained, relative to the material properties of gels, poorly characterized. We envision that the methods used here will prove to be useful tools for elucidating the effects that various factors, such as peptide sequence and solution conditions, have on hydrogelation.

ASSOCIATED CONTENT

Supporting Information

The Supporting Information is available free of charge at https://pubs.acs.org/doi/10.1021/acs.biomac.0c00989.

Estimation of the elongation rate (k_+), mass spectrometry of SgI_{37-49}, peptide purification by HPLC and SEC, ThT calibration, and seeded kinetic aggregation (PDF)

AUTHOR INFORMATION

Corresponding Authors

Gabriel A. Braun − *Department of Chemistry, Haverford College, Haverford, Pennsylvania 19041, United States; Department of Biochemistry and Structural Biology, Centre for Molecular Protein Science, Lund University, Lund SE-22100, Sweden;* orcid.org/0000-0002-9105-5757; Email: gabriel.braun@fulbrightmail.org

Sara Linse − *Department of Biochemistry and Structural Biology, Centre for Molecular Protein Science, Lund University, Lund SE-22100, Sweden;* orcid.org/0000-0001-9629-7109; Email: sara.linse@biochemistry.lu.se

Karin S. Åkerfeldt − *Department of Chemistry, Haverford College, Haverford, Pennsylvania 19041, United States;* Email: kakerfel@haverford.edu

Authors

Beatrice E. Ary − *Department of Chemistry, Haverford College, Haverford, Pennsylvania 19041, United States*

Alexander J. Dear − *Department of Chemistry, University of Cambridge, Cambridge CB2 1EW, U.K.; Paulson School of Engineering and Applied Science, Harvard University, Cambridge, Massachusetts 02138, United States*

Matthew C. H. Rohn − *Department of Chemistry, Haverford College, Haverford, Pennsylvania 19041, United States*

Abigail M. Payson − *Department of Chemistry, Haverford College, Haverford, Pennsylvania 19041, United States*

David S. M. Lee − *Department of Chemistry, Haverford College, Haverford, Pennsylvania 19041, United States*

Robert C. Parry − *Department of Chemistry, Haverford College, Haverford, Pennsylvania 19041, United States*

Connie Friedman − *Department of Chemistry, Haverford College, Haverford, Pennsylvania 19041, United States*

Tuomas P. J. Knowles − *Department of Chemistry and Cavendish Laboratory, University of Cambridge, Cambridge CB2 1EW, U.K.;* orcid.org/0000-0002-7879-0140

Complete contact information is available at: https://pubs.acs.org/10.1021/acs.biomac.0c00989

Notes

The authors declare no competing financial interest.

ACKNOWLEDGMENTS

We gratefully acknowledge Sarah Figueredo and Gunnel Karlsson for the preparation and imaging of the cryo-TEM samples, respectively, as well as Shelby Lyons for her early contributions to the development of the ThT assay. We sincerely thank Drs. Casey Londergan and Lou Charkoudian for the use of their FTIR and LCMS instruments, respectively. This work was supported by funding from Haverford College (K.S.Å.); the National Science Foundation Division of Chemistry, Macromolecular, Supramolecular, and Nanochemistry Program grant CHE-1609291 (K.S.Å.); the Swedish Research Council grant 2015-00143 (S.L.); the Fulbright U.S. Student Program (G.A.B.); the Lindemann Trust Fellowship (A.J.D.); the Novo Nordisk Foundation (A.J.D.); and the Frances and Augustus Newman Foundation (T.P.J.K.). The research leading to these results has received funding from the European Research Council under the European Union's Seventh Framework Programme (FP7/2007−2013) through the ERC grant PhysProt (agreement no. 337969).

REFERENCES

(1) Zhang, Y. S.; Khademhosseini, A. Advances in Engineering Hydrogels. *Science* **2017**, *356*, No. eaaf3627.

(2) Montheil, T.; Echalier, C.; Martinez, J.; Subra, G.; Mehdi, A. Inorganic Polymerization: An Attractive Route to Biocompatible Hybrid Hydrogels. *J. Mater. Chem. B* **2018**, *6*, 3434−3448.

(3) Du, X.; Zhou, J.; Shi, J.; Xu, B. Supramolecular Hydrogelators and Hydrogels: From Soft Matter to Molecular Biomaterials. *Chem. Rev.* **2015**, *115*, 13165−13307.

(4) Carlini, A. S.; Adamiak, L.; Gianneschi, N. C. Biosynthetic Polymers as Functional Materials. *Macromolecules* **2016**, *49*, 4379−4394.

(5) Zhou, J.; Li, J.; Du, X.; Xu, B. Supramolecular Biofunctional Materials. *Biomaterials* **2017**, *129*, 1−27.
(6) Liu, Y.; Hsu, S. Synthesis and Biomedical Applications of Self-Healing Hydrogels. *Front. Chem.* **2018**, *6*, 449.
(7) Li, J.; Xing, R.; Bai, S.; Yan, X. Recent Advances of Self-Assembling Peptide-Based Hydrogels for Biomedical Applications. *Soft Matter* **2019**, *15*, 1704−1715.
(8) Bowerman, C. J.; Nilsson, B. L. Review self-assembly of amphipathic β-sheet peptides: Insights and applications. *Biopolymers* **2012**, *98*, 169−184.
(9) Frohm, B.; DeNizio, J. E.; Lee, D. S. M.; Gentile, L.; Olsson, U.; Malm, J.; Åkerfeldt, K. S.; Linse, S. A Peptide from Human Semenogelin I Self-Assembles into a PH-Responsive Hydrogel. *Soft Matter* **2015**, *11*, 414−421.
(10) Aggeli, A.; Bell, M.; Boden, N.; Keen, J. N.; Knowles, P. F.; McLeish, T. C. B.; Pitkeathly, M.; Radford, S. E. Responsive gels formed by the spontaneous self-assembly of peptides into polymeric β-sheet tapes. *Nature* **1997**, *386*, 259−262.
(11) Yokoi, H.; Kinoshita, T.; Zhang, S. Dynamic Reassembly of Peptide RADA16 Nanofiber Scaffold. *Proc. Natl. Acad. Sci. U.S.A.* **2005**, *102*, 8414−8419.
(12) Wu, D.; Zhang, S.; Zhao, Y.; Ao, N.; Ramakrishna, S.; He, L. The Effects of Motif Net Charge and Amphiphilicity on the Self-Assembly of Functionally Designer RADA16-I Peptides. *Biomed. Mater.* **2018**, *13*, 035011.
(13) Hong, Y.; Legge, R. L.; Zhang, S.; Chen, P. Effect of Amino Acid Sequence and PH on Nanofiber Formation of Self-Assembling Peptides EAK16-II and EAK16-IV. *Biomacromolecules* **2003**, *4*, 1433−1442.
(14) Schneider, J. P.; Pochan, D. J.; Ozbas, B.; Rajagopal, K.; Pakstis, L.; Kretsinger, J. Responsive Hydrogels from the Intramolecular Folding and Self-Assembly of a Designed Peptide. *J. Am. Chem. Soc.* **2002**, *124*, 15030−15037.
(15) Worthington, P.; Langhans, S.; Pochan, D. β-hairpin peptide hydrogels for package delivery. *Adv. Drug Deliv. Rev.* **2017**, *110-111*, 127−136.
(16) Aggeli, A.; Nyrkova, I. A.; Bell, M.; Harding, R.; Carrick, L.; McLeish, T. C. B.; Semenov, A. N.; Boden, N. Hierarchical Self-Assembly of Chiral Rod-like Molecules as a Model for Peptide -Sheet Tapes, Ribbons, Fibrils, and Fibers. *Proc. Natl. Acad. Sci. U.S.A.* **2001**, *98*, 11857−11862.
(17) Kyle, S.; Felton, S. H.; McPherson, M. J.; Aggeli, A.; Ingham, E. Rational Molecular Design of Complementary Self-Assembling Peptide Hydrogels. *Adv. Healthcare Mater.* **2012**, *1*, 640−645.
(18) Maude, S.; Ingham, E.; Aggeli, A. Biomimetic Self-Assembling Peptides as Scaffolds for Soft Tissue Engineering. *Nanomedicine* **2013**, *8*, 823−847.
(19) Wei, G.; Su, Z.; Reynolds, N. P.; Arosio, P.; Hamley, I. W.; Gazit, E.; Mezzenga, R. Self-Assembling Peptide and Protein Amyloids: From Structure to Tailored Function in Nanotechnology. *Chem. Soc. Rev.* **2017**, *46*, 4661−4708.
(20) Zhang, S. Discovery and Design of Self-Assembling Peptides. *Interface Focus* **2017**, *7*, 20170028.
(21) Nagarkar, RP.; Schneider, JP. Synthesis and Primary Characterization of Self-Assembled Peptide-Based Hydrogels. In *Nanostructure Design*; Gazit, E.; Nussinov, R.; Walker, J. M., Eds.; Methods in Molecular Biology; Humana Press: Totowa, NJ, 2008; Vol. *474*, pp 61−77. DOI: 10.1007/978-1-59745-480-3_5
(22) Yan, C.; Pochan, D. J. Rheological Properties of Peptide-Based Hydrogels for Biomedical and Other Applications. *Chem. Soc. Rev.* **2010**, *39*, 3528.
(23) Guilbaud, J.-B.; Saiani, A. Using Small Angle Scattering (SAS) to Structurally Characterise Peptide and Protein Self-Assembled Materials. *Chem. Soc. Rev.* **2011**, *40*, 1200−1210.
(24) De Leon Rodriguez, L. M.; Hemar, Y.; Cornish, J.; Brimble, M. A. Structure-mechanical property correlations of hydrogel forming β-sheet peptides. *Chem. Soc. Rev.* **2016**, *45*, 4797−4824.
(25) Wang, J.; Liu, K.; Xing, R.; Yan, X. Peptide Self-Assembly: Thermodynamics and Kinetics. *Chem. Soc. Rev.* **2016**, *45*, 5589−5604.
(26) Raymond, D. M.; Nilsson, B. L. Multicomponent Peptide Assemblies. *Chem. Soc. Rev.* **2018**, *47*, 3659−3720.
(27) Xiong, J.-Y.; Narayanan, J.; Liu, X.-Y.; Chong, T. K.; Chen, S. B.; Chung, T.-S. Topology Evolution and Gelation Mechanism of Agarose Gel. *J. Phys. Chem. B* **2005**, *109*, 5638−5643.
(28) Martin, A. D.; Wojciechowski, J. P.; Warren, H.; in het Panhuis, M.; Thordarson, P. Effect of Heterocyclic Capping Groups on the Self-Assembly of a Dipeptide Hydrogel. *Soft Matter* **2016**, *12*, 2700−2707.
(29) Larsen, T. H.; Branco, M. C.; Rajagopal, K.; Schneider, J. P.; Furst, E. M. Sequence-Dependent Gelation Kinetics of β-Hairpin Peptide Hydrogels. *Macromolecules* **2009**, *42*, 8443−8450.
(30) Chen, L.; Morris, K.; Laybourn, A.; Elias, D.; Hicks, M. R.; Rodger, A.; Serpell, L.; Adams, D. J. Self-Assembly Mechanism for a Naphthalene−Dipeptide Leading to Hydrogelation. *Langmuir* **2010**, *26*, 5232−5242.
(31) Jean, L.; Lee, C. F.; Hodder, P.; Hawkins, N.; Vaux, D. J. Dynamics of the Formation of a Hydrogel by a Pathogenic Amyloid Peptide: Islet Amyloid Polypeptide. *Sci. Rep.* **2016**, *6*, 32124.
(32) Haines-Butterick, L.; Rajagopal, K.; Branco, M.; Salick, D.; Rughani, R.; Pilarz, M.; Lamm, M. S.; Pochan, D. J.; Schneider, J. P. Controlling Hydrogelation Kinetics by Peptide Design for Three-Dimensional Encapsulation and Injectable Delivery of Cells. *Proc. Natl. Acad. Sci. U.S.A.* **2007**, *104*, 7791−7796.
(33) Veerman, C.; Rajagopal, K.; Palla, C. S.; Pochan, D. J.; Schneider, J. P.; Furst, E. M. Gelation Kinetics of β-Hairpin Peptide Hydrogel Networks. *Macromolecules* **2006**, *39*, 6608−6614.
(34) DiGuiseppi, D.; Kraus, J.; Toal, S. E.; Alvarez, N.; Schweitzer-Stenner, R. Investigating the Formation of a Repulsive Hydrogel of a Cationic 16mer Peptide at Low Ionic Strength in Water by Vibrational Spectroscopy and Rheology. *J. Phys. Chem. B* **2016**, *120*, 10079−10090.
(35) Bolder, S. G.; Sagis, L. M. C.; Venema, P.; van der Linden, E. Thioflavin T and Birefringence Assays to Determine the Conversion of Proteins into Fibrils. *Langmuir* **2007**, *23*, 4144−4147.
(36) Fichman, G.; Gazit, E. Self-Assembly of Short Peptides to Form Hydrogels: Design of Building Blocks, Physical Properties and Technological Applications. *Acta Biomater.* **2014**, *10*, 1671−1682.
(37) De Leon-Rodriguez, L. M.; Hemar, Y.; Mitra, A. K.; Brimble, M. A. Understanding the metal mediated assembly and hydrogel formation of a β-hairpin peptide. *Biomater. Sci.* **2017**, *5*, 1993−1997.
(38) Wang, L.; Shi, X.; Wu, Y.; Zhang, J.; Zhu, Y.; Wang, J. A Multifunctional Supramolecular Hydrogel: Preparation, Properties and Molecular Assembly. *Soft Matter* **2018**, *14*, 566−573.
(39) Singha, N.; Srivastava, A.; Pramanik, B.; Ahmed, S.; Dowari, P.; Chowdhuri, S.; Das, B. K.; Debnath, A.; Das, D. Unusual Confinement Properties of a Water Insoluble Small Peptide Hydrogel. *Chem. Sci.* **2019**, *10*, 5920−5928.
(40) Tena-Solsona, M.; Miravet, J. F.; Escuder, B. Tetrapeptidic Molecular Hydrogels: Self-assembly and Co-aggregation with Amyloid Fragment Aβ1-40. *Chem.—Eur. J.* **2014**, *20*, 1023−1031.
(41) Caplan, M. R.; Moore, P. N.; Zhang, S.; Kamm, R. D.; Lauffenburger, D. A. Self-Assembly of a β-Sheet Protein Governed by Relief of Electrostatic Repulsion Relative to van der Waals Attraction. *Biomacromolecules* **2000**, *1*, 627−631.
(42) Veerman, C.; Ruis, H.; Sagis, L. M. C.; van der Linden, E. Effect of Electrostatic Interactions on the Percolation Concentration of Fibrillar β-Lactoglobulin Gels. *Biomacromolecules* **2002**, *3*, 869−873.
(43) Aggeli, A.; Bell, M.; Carrick, L. M.; Fishwick, C. W. G.; Harding, R.; Mawer, P. J.; Radford, S. E.; Strong, A. E.; Boden, N. pH as a Trigger of Peptide β-Sheet Self-Assembly and Reversible Switching between Nematic and Isotropic Phases. *J. Am. Chem. Soc.* **2003**, *125*, 9619−9628.
(44) Bolisetty, S.; Harnau, L.; Jung, J.-m.; Mezzenga, R. Gelation, Phase Behavior, and Dynamics of β-Lactoglobulin Amyloid Fibrils at Varying Concentrations and Ionic Strengths. *Biomacromolecules* **2012**, *13*, 3241−3252.

https://dx.doi.org/10.1021/acs.biomac.0c00989
Biomacromolecules XXXX, XXX, XXX−XXX

(45) Arosio, P.; Knowles, T. P. J.; Linse, S. On the Lag Phase in Amyloid Fibril Formation. *Phys. Chem. Chem. Phys.* **2015**, *17*, 7606−7618.
(46) Arosio, P.; Cukalevski, R.; Frohm, B.; Knowles, T. P. J.; Linse, S. Quantification of the Concentration of Aβ42 Propagons during the Lag Phase by an Amyloid Chain Reaction Assay. *J. Am. Chem. Soc.* **2014**, *136*, 219−225.
(47) Tena-Solsona, M.; Escuder, B.; Miravet, J. F.; Casttelleto, V.; Hamley, I. W.; Dehsorkhi, A. Thermodynamic and Kinetic Study of the Fibrillization of a Family of Tetrapeptides and Its Application to Self-Sorting. What Takes So Long? *Chem. Mater.* **2015**, *27*, 3358−3365.
(48) Dudukovic, N. A.; Zukoski, C. F. Gelation of Fmoc-Diphenylalanine Is a First Order Phase Transition. *Soft Matter* **2015**, *11*, 7663−7673.
(49) Laishram, R.; Maitra, U. Supramolecular Gelation of Europium and Calcium Cholates through the Nucleation-Elongation Growth Mechanism. *ChemPlusChem* **2019**, *84*, 853−861.
(50) Zhang, H.; Luo, H.; Zhao, X. Mechanistic Study of Self-Assembling Peptide RADA16-I in Formation of Nanofibers and Hydrogels. *J. Nanotechnol. Eng. Med* **2010**, *1*, 011007.
(51) Emamyari, S.; Kargar, F.; Sheikh-hasani, V.; Emadi, S.; Fazli, H. Mechanisms of the Self-Assembly of EAK16-Family Peptides into Fibrillar and Globular Structures: Molecular Dynamics Simulations from Nano- to Micro-Seconds. *Eur. Biophys. J.* **2015**, *44*, 263−276.
(52) Pandya, M. J.; Spooner, G. M.; Sunde, M.; Thorpe, J. R.; Rodger, A.; Woolfson, D. N. Sticky-End Assembly of a Designed Peptide Fiber Provides Insight into Protein Fibrillogenesis†. *Biochemistry* **2000**, *39*, 8728−8734.
(53) Lara, C.; Adamcik, J.; Jordens, S.; Mezzenga, R. General Self-Assembly Mechanism Converting Hydrolyzed Globular Proteins Into Giant Multistranded Amyloid Ribbons. *Biomacromolecules* **2011**, *12*, 1868−1875.
(54) Michaels, T. C. T.; Liu, L. X.; Meisl, G.; Knowles, T. P. J. Physical Principles of Filamentous Protein Self-Assembly Kinetics. *J. Phys. Condens. Matter* **2017**, *29*, 153002.
(55) Kumar, E. K.; Haque, N.; Prabhu, N. P. Kinetics of Protein Fibril Formation: Methods and Mechanisms. *Int. J. Biol. Macromol.* **2017**, *100*, 3−10.
(56) *Biological and Bio-Inspired Nanomaterials: Properties and Assembly Mechanisms*; Perrett, S.; Buell, A. K.; Knowles, T. P. J., Eds.; Advances in Experimental Medicine and Biology; Springer Singapore: Singapore, 2019; Vol. *1174*.
(57) Hofrichter, J.; Ross, P. D.; Eaton, W. A. Kinetics and Mechanism of Deoxyhemoglobin S Gelation: A New Approach to Understanding Sickle Cell Disease. *Proc. Natl. Acad. Sci. U.S.A.* **1974**, *71*, 4864−4868.
(58) Behe, M. J.; Englander, S. W. Sickle Hemoglobin Gelation. Reaction Order and Critical Nucleus Size. *Biophys. J.* **1978**, *23*, 129−145.
(59) Adachi, K.; Matarasso, S. L.; Asakura, T. Nucleation-Controlled Aggregation of Deoxyhemoglobin S Effect of Organic Phosphates on the Kinetics of Aggregation of Deoxyhemoglobin S in Concentrated Phosphate Buffer. *Biochim. Biophys. Acta, Protein Struct. Mol. Enzymol.* **1980**, *624*, 372−377.
(60) Ferrone, F. A.; Hofrichter, J.; Sunshine, H. R.; Eaton, W. A. Kinetic Studies on Photolysis-Induced Gelation of Sickle Cell Hemoglobin Suggest a New Mechanism. *Biophys. J.* **1980**, *32*, 361−380.
(61) Cohen, S. I. A.; Linse, S.; Luheshi, L. M.; Hellstrand, E.; White, D. A.; Rajah, L.; Otzen, D. E.; Vendruscolo, M.; Dobson, C. M.; Knowles, T. P. J. Proliferation of Amyloid- 42 Aggregates Occurs through a Secondary Nucleation Mechanism. *Proc. Natl. Acad. Sci. U.S.A.* **2013**, *110*, 9758−9763.
(62) Meisl, G.; Yang, X.; Hellstrand, E.; Frohm, B.; Kirkegaard, J. B.; Cohen, S. I. A.; Dobson, C. M.; Linse, S.; Knowles, T. P. J. Differences in nucleation behavior underlie the contrasting aggregation kinetics of the Aβ40 and Aβ42 peptides. *Proc. Natl. Acad. Sci. U.S.A.* **2014**, *111*, 9384−9389.
(63) Buell, A. K.; Galvagnion, C.; Gaspar, R.; Sparr, E.; Vendruscolo, M.; Knowles, T. P. J.; Linse, S.; Dobson, C. M. Solution Conditions Determine the Relative Importance of Nucleation and Growth Processes in -Synuclein Aggregation. *Proc. Natl. Acad. Sci. U.S.A.* **2014**, *111*, 7671−7676.
(64) Shammas, S. L.; Garcia, G. A.; Kumar, S.; Kjaergaard, M.; Horrocks, M. H.; Shivji, N.; Mandelkow, E.; Knowles, T. P. J.; Mandelkow, E.; Klenerman, D. A Mechanistic Model of Tau Amyloid Aggregation Based on Direct Observation of Oligomers. *Nat. Commun.* **2015**, *6*, 7025.
(65) Chen, S.; Ferrone, F. A.; Wetzel, R. Huntington's disease age-of-onset linked to polyglutamine aggregation nucleation. *Proc. Natl. Acad. Sci. U.S.A.* **2002**, *99*, 11884−11889.
(66) Bhattacharyya, A. M.; Thakur, A. K.; Wetzel, R. Polyglutamine Aggregation Nucleation: Thermodynamics of a Highly Unfavorable Protein Folding Reaction. *Proc. Natl. Acad. Sci. U.S.A.* **2005**, *102*, 15400−15405.
(67) Carbonell, F.; Iturria-Medina, Y.; Evans, A. C. Mathematical Modeling of Protein Misfolding Mechanisms in Neurological Diseases: A Historical Overview. *Front. Neurol.* **2018**, *9*, 37.
(68) Chatani, E.; Yamamoto, N. Recent Progress on Understanding the Mechanisms of Amyloid Nucleation. *Proc. Natl. Acad. Sci. U.S.A.* **2018**, *10*, 527−534.
(69) Michaels, T. C. T.; Šarić, A.; Habchi, J.; Chia, S.; Meisl, G.; Vendruscolo, M.; Dobson, C. M.; Knowles, T. P. J. Chemical Kinetics for Bridging Molecular Mechanisms and Macroscopic Measurements of Amyloid Fibril Formation. *Annu. Rev. Phys. Chem.* **2018**, *69*, 273−298.
(70) Meisl, G.; Kirkegaard, J. B.; Arosio, P.; Michaels, T. C. T.; Vendruscolo, M.; Dobson, C. M.; Linse, S.; Knowles, T. P. J. Molecular Mechanisms of Protein Aggregation from Global Fitting of Kinetic Models. *Nat. Protoc.* **2016**, *11*, 252−272.
(71) Dear, A. J.; Meisl, G.; Michaels, T. C. T.; Zimmermann, M. R.; Linse, S.; Knowles, T. P. J. The Catalytic Nature of Protein Aggregation. *J. Chem. Phys.* **2020**, *152*, 045101.
(72) Kubelka, J.; Keiderling, T. A. The Anomalous Infrared Amide I Intensity Distribution in13C Isotopically Labeled Peptide β-Sheets Comes from Extended, Multiple-Stranded Structures. An ab Initio Study. *J. Am. Chem. Soc.* **2001**, *123*, 6142−6150.
(73) Decatur, S. M. Elucidation of Residue-Level Structure and Dynamics of Polypeptides via Isotope-Edited Infrared Spectroscopy. *Acc. Chem. Res.* **2006**, *39*, 169−175.
(74) Gurry, T.; Stultz, C. M. Mechanism of Amyloid-β Fibril Elongation. *Biochemistry* **2014**, *53*, 6981−6991.
(75) Scheidt, T.; Łapińska, U.; Kumita, J. R.; Whiten, D. R.; Klenerman, D.; Wilson, M. R.; Cohen, S. I. A.; Linse, S.; Vendruscolo, M.; Dobson, C. M.; Knowles, T. P. J.; Arosio, P. Secondary nucleation and elongation occur at different sites on Alzheimer's amyloid-β aggregates. *Sci. Adv.* **2019**, *5*, No. eaau3112.
(76) Buell, A. K. The Nucleation of Protein Aggregates - From Crystals to Amyloid Fibrils. In *International Review of Cell and Molecular Biology*; Elsevier, 2017; Vol. *329*, pp 187−226. https://doi.org/10.1016/bs.ircmb.2016.08.014. DOI: 10.1016/bs.ircmb.2016.08.014
(77) Törnquist, M.; Michaels, T. C. T.; Sanagavarapu, K.; Yang, X.; Meisl, G.; Cohen, S. I. A.; Knowles, T. P. J.; Linse, S. Secondary Nucleation in Amyloid Formation. *Chem. Commun.* **2018**, *54*, 8667−8684.
(78) Xue, W.-F.; Homans, S. W.; Radford, S. E. Systematic Analysis of Nucleation-Dependent Polymerization Reveals New Insights into the Mechanism of Amyloid Self-Assembly. *Proc. Natl. Acad. Sci. U.S.A.* **2008**, *105*, 8926−8931.
(79) Powers, E. T.; Powers, D. L. Mechanisms of Protein Fibril Formation: Nucleated Polymerization with Competing Off-Pathway Aggregation. *Biophys. J.* **2008**, *94*, 379−391.
(80) Dovidchenko, N. V.; Finkelstein, A. V.; Galzitskaya, O. V. How to Determine the Size of Folding Nuclei of Protofibrils from the Concentration Dependence of the Rate and Lag-Time of Aggregation.

https://dx.doi.org/10.1021/acs.biomac.0c00989
Biomacromolecules XXXX, XXX, XXX−XXX

I. Modeling the Amyloid Protofibril Formation. *J. Phys. Chem. B* **2014**, *118*, 1189−1197.
(81) Cohen, S. I. A.; Vendruscolo, M.; Dobson, C. M.; Knowles, T. P. J. The Kinetics and Mechanisms of Amyloid Formation. In *Amyloid Fibrils and Prefibrillar Aggregates*; Otzen, D. E., Ed.; Wiley-VCH Verlag GmbH & Co. KGaA: Weinheim, Germany, 2013; pp 183−209.
(82) Cohen, S. I. A.; Arosio, P.; Presto, J.; Kurudenkandy, F. R.; BiverstÅl, H.; Dolfe, L.; Dunning, C.; Yang, X.; Frohm, B.; Vendruscolo, M.; Johansson, J.; Dobson, C. M.; Fisahn, A.; Knowles, T. P. J.; Linse, S. A molecular chaperone breaks the catalytic cycle that generates toxic Aβ oligomers. *Nat. Struct. Mol. Biol.* **2015**, *22*, 207−213.
(83) Dear, A. J.; Michaels, T. C. T.; Meisl, G.; Klenerman, D.; Wu, S.; Perrett, S.; Linse, S.; Dobson, C. M.; Knowles, T. P. J. Kinetic Diversity of Amyloid Oligomers. *Proc. Natl. Acad. Sci. U.S.A.* **2020**, *117*, 12087−12094.
(84) Šarić, A.; Buell, A. K.; Meisl, G.; Michaels, T. C. T.; Dobson, C. M.; Linse, S.; Knowles, T. P. J.; Frenkel, D. Physical Determinants of the Self-Replication of Protein Fibrils. *Nat. Phys.* **2016**, *12*, 874−880.
(85) Carlier, M. F.; Pantaloni, D. Kinetic Analysis of Cooperativity in Tubulin Polymerization in the Presence of Guanosine Di- or Triphosphate Nucleotides. *Biochemistry* **1978**, *17*, 1908−1915.
(86) Kar, K.; Jayaraman, M.; Sahoo, B.; Kodali, R.; Wetzel, R. Critical Nucleus Size for Disease-Related Polyglutamine Aggregation Is Repeat-Length Dependent. *Nat. Struct. Mol. Biol.* **2011**, *18*, 328−336.
(87) Galkin, O.; Vekilov, P. G. Mechanisms of Homogeneous Nucleation of Polymers of Sickle Cell Anemia Hemoglobin in Deoxy State. *J. Mol. Biol.* **2004**, *336*, 43−59.
(88) Linse, S. Monomer-Dependent Secondary Nucleation in Amyloid Formation. *Biophys. Rev.* **2017**, *9*, 329−338.
(89) Ramachandran, S.; Tseng, Y.; Yu, Y. B. Repeated Rapid Shear-Responsiveness of Peptide Hydrogels with Tunable Shear Modulus. *Biomacromolecules* **2005**, *6*, 1316−1321.
(90) Yan, C.; Altunbas, A.; Yucel, T.; Nagarkar, R. P.; Schneider, J. P.; Pochan, D. J. Injectable solid hydrogel: mechanism of shear-thinning and immediate recovery of injectable β-hairpin peptide hydrogels. *Soft Matter* **2010**, *6*, 5143.
(91) Morriss-Andrews, A.; Bellesia, G.; Shea, J.-E. β-sheet propensity controls the kinetic pathways and morphologies of seeded peptide aggregation. *J. Chem. Phys.* **2012**, *137*, 145104.
(92) Vácha, R.; Linse, S.; Lund, M. Surface Effects on Aggregation Kinetics of Amyloidogenic Peptides. *J. Am. Chem. Soc.* **2014**, *136*, 11776−11782.
(93) Morinaga, A.; Hasegawa, K.; Nomura, R.; Ookoshi, T.; Ozawa, D.; Goto, Y.; Yamada, M.; Naiki, H. Critical role of interfaces and agitation on the nucleation of Aβ amyloid fibrils at low concentrations of Aβ monomers. *Biochim. Biophys. Acta, Proteins Proteomics* **2010**, *1804*, 986−995.
(94) Jean, L.; Lee, C. F.; Vaux, D. J. Enrichment of Amyloidogenesis at an Air-Water Interface. *Biophys. J.* **2012**, *102*, 1154−1162.
(95) Risør, M. W.; Juhl, D. W.; Bjerring, M.; Mathiesen, J.; Enghild, J. J.; Nielsen, N. C.; Otzen, D. E. Critical Influence of Cosolutes and Surfaces on the Assembly of Serpin-Derived Amyloid Fibrils. *Biophys. J.* **2017**, *113*, 580−596.
(96) Grigolato, F.; Colombo, C.; Ferrari, R.; Rezabkova, L.; Arosio, P. Mechanistic Origin of the Combined Effect of Surfaces and Mechanical Agitation on Amyloid Formation. *ACS Nano* **2017**, *11*, 11358−11367.

https://dx.doi.org/10.1021/acs.biomac.0c00989
Biomacromolecules XXXX, XXX, XXX−XXX